Earthquake Research Advances 6 (2026) 100390

Contents lists available at ScienceDirect

Earthquake Research Advances

journal homepage: www.keaipublishing.com/en/journals/earthquake-research-advances

The seismogenic structure of strong intraplate earthquakes in Shantou region, South China: Insights from upper crustal shear-wave velocity structure

Lue Yang [a], Lun Li [a,*], Xiuwei Ye [b,c,d], Jinming Zhang [a], Jialong He [a], Yuan Gao [a], Pengfei Li [a], Yu He [a], Ziwei Li [a]

[a] School of Earth Sciences and Engineering, Sun Yat-Sen University, and Southern Marine Science and Engineering Guangdong Laboratory, Zhuhai, 519082, China
[b] China Earthquake Administration Key Laboratory of Earthquake Monitoring and Disaster Mitigation Technology, Guangdong Earthquake Agency, Guangzhou, 510070, China
[c] Guangdong Science and Technology Collaborative Innovation Center for Earthquake Prevention and Disaster Mitigation, Guangzhou, 510070, China
[d] Key Laboratory of Disaster Forecast and Control in Engineering of the Ministry of Education, Urban Earthquake Safety Laboratory, Guangzhou, 510070, China

ARTICLE INFO

Keywords:
Intraplate earthquakes
Nan'ao earthquake
Shear-wave velocity
Ambient noise tomography
Dense seismic array

ABSTRACT

The Shantou region, one of the most seismically active zones of Guangdong Province (South China), has experienced multiple strong earthquakes, including two significant events with magnitudes greater than 7.0 that occurred in 1600 and 1918, respectively. To investigate the seismogenic structures responsible for these major earthquakes and their potential triggering mechanisms, we construct a high-resolution shear-wave velocity model from the surface to ~15 km depth based on a dense nodal seismic array using ambient noise tomography. The model reveals a pronounced low-velocity zone (LVZ) at depths of 2–15 km, with a perturbation of −2 to −8%, coinciding with the northwestern extension of the Huanggangshui Fault previously identified in the offshore region. Integrating our results with previous field geological surveys and shallow reflection seismic exploration, we interpret the LVZ as a wide fault zone, potentially comprising multiple fault branches that possibly include two NW-trending faults (i.e., the Rongjiang Fault and the Hanjiang Fault). Notably, the interaction between the Huanggangshui Fault and NE-trending Littoral Fault is suggested to have triggered the 1918 M 7.3 Nan'ao earthquake. Additionally, the 1895 M 6.2 earthquake seems to have occurred at the edge of the LVZ near the Rongjiang Fault, a possible branch of the Huanggangshui Fault, further supporting the association between this structure and seismic activity. These findings imply that the LVZ may represent a region of concentrated tectonic stress, making it a potential site for future strong earthquakes. Consequently, this area should be prioritized in seismic hazard assessments. This study provides valuable insights into the seismogenic characteristics of the Shantou region and contributes to improving seismic hazard evaluations in South China.

1. Introduction

The frequent occurrence of intraplate strong earthquakes is well documented in China (Zhang et al., 2003). Approximately 80%–90% of China's strong earthquakes with magnitudes of 7 or greater are concentrated at the boundaries of active tectonic blocks, with the remaining 10%–20% occurring within these blocks (Zhang et al., 2003). Over the past few decades, substantial research efforts have primarily focused on understanding the triggering mechanisms of earthquakes at block boundaries (Zhang et al., 2003; Ma, 1999; Zheng et al., 2022), while the strong earthquakes within the blocks have received comparatively less attention.

Guangdong Province, situated in the southern portion of the stable South China Block, exhibits higher seismicity than other areas within the South China Block (Liu, 2001). The Shantou region in eastern Guangdong Province is recognized as one of the most seismically active zones in the province (Fig. 1a). Historical records indicate that the Shantou region has experienced multiple strong earthquakes with magnitudes greater than 6.0, including two significant seismic events with $M > 7.0$ that occurred in 1600 and 1918 (Fig. 1) (Chen and Huang, 1984). Among them, the 1918

* Corresponding author.
E-mail addresses: lilun6@mail.sysu.edu.cn, lilun.cugb@gmail.com (L. Li).
Peer review under the responsibility of Editorial Board of Earthquake Research Advances.

https://doi.org/10.1016/j.eqrea.2025.100390
Received 8 December 2024; Received in revised form 30 March 2025; Accepted 17 April 2025

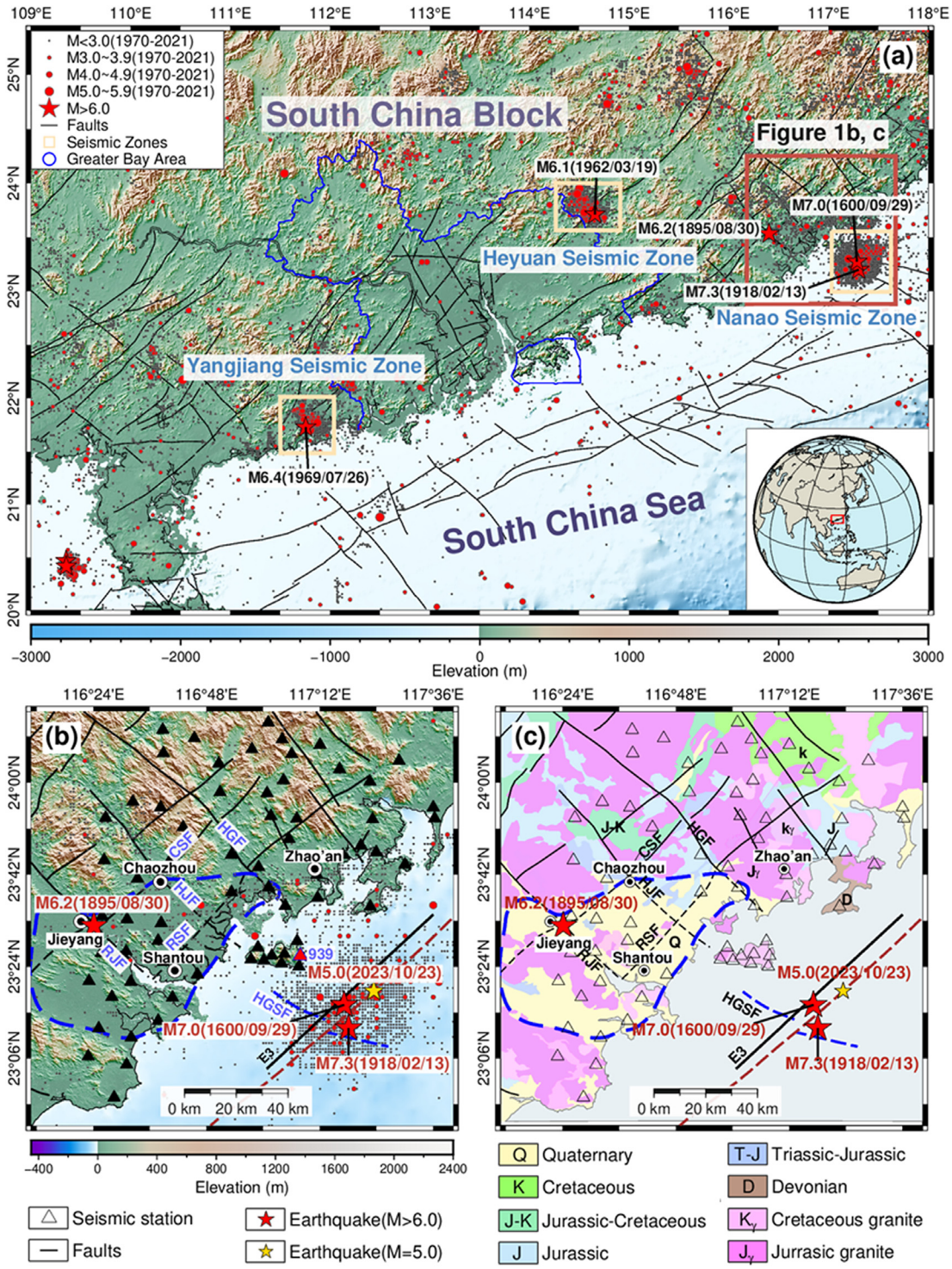

Fig. 1. (a) Topography map of Guangdong Province, South China, overlaid with seismicity data from 1970 to 2021 (Guangdong Earthquake Agency, China). The inset map shows the location of panel (a). The light-yellow rectangles indicate the seismically active zones (i.e., the Nan'ao Seismic Zone). Black lines represent fault lines from Deng (2007) and Ye et al. (2024). The blue line outlines the boundary of the Guangdong-Hong Kong-Macao Greater Bay Area, South China. Red stars mark historical earthquakes with magnitudes larger than 6.0 in Guangdong Province (Guangdong Earthquake Agency, China). (b) Topographic map of the Shantou region overlaid with seismicity data. The location of this map is indicated in panel (a). Black triangles denote seismic stations, while the red triangle represents the seismic station shown in Fig. 3. Brown and blue dashed lines correspond to the Littoral Fault Zone (Xie et al., 2015) and the Huanggangshui Fault (HGSF) (Xia et al., 2020), respectively. The black solid line (E3) represents the location of the seismic reflection profile from Xia et al. (2020). The red stars mark historical earthquakes with magnitudes larger than 6.0 in the Shantou region (Xu et al., 2006; Xia et al., 2020; Chen and Huang, 1984). The gold star denotes a magnitude 5.0 earthquake that occurred in the Shantou region on October 23, 2023. (c) Geological map of the Shantou region (modified from the 1:1,000,000 geological map of China). The blue dashed line denotes the approximate range of the Chaoshan Basin. The legends are provided at the bottom of the figure. RJF: the Rongjiang Fault. HJF: the Hanjiang Fault. HGF: the Huangganghe Fault. CSF: the Chaozhou-Shanwei Fault. RSF: the Raoping-Shantou Fault.

earthquake has an estimated magnitude of 7.3 (Wei et al., 2001).

Geological and seismic surveys on the 1918 earthquake suggested a focal depth ranging from 15 km to 18 km (Xu et al., 2006; Xia et al., 2020) with large uncertainties since there are no direct seismic observations. This earthquake even triggered a tsunami, causing significant casualties and property damage in Nan'ao Island of the Shantou region (Xu et al., 2006; Li et al., 2022). Previous studies on focal mechanism, seismicity, and fault system indicated that the 1918 Nan'ao earthquake was intricately linked to the movement of the ENE-trending Littoral fault zone (Zhao et al., 2004; Xu et al., 2010; Xia et al., 2020; Li et al., 2022; Hui et al., 2022; Zhang et al., 2024) and its interaction with the NW-trending Huanggangshui fault (Xu et al., 2006; Xia et al., 2020, Fig. 1b and c).

Based on a detailed analysis of the isoseismal contour distribution of seismic intensity of the 1918 Nan'ao earthquake, Xu et al. (2006) identified the Littoral Fault Zone as the primary seismogenic structure, with the Huanggangshui Fault playing a secondary role. They further proposed that the Huanggangshui Fault may extend southeastward, potentially connecting with the Taiwan Narrow Fault, making it a key fault system associated with major seismic events, such as the 1918 Nan'ao *M* 7.3 earthquake and the 1994 Taiwan Strait *M* 7.3 earthquake, China (Xu et al., 2006). Given this potential linkage, mapping the onshore extension of the Huanggangshui Fault is critical for assessing seismic hazards in the Shantou region. Xu et al. (2006) suggested that the offshore segment of the Huanggangshui Fault is located north of Nan'ao Island and connects with the Huangganghe Fault on land. However, Xia et al. (2020), using seismic reflection profiles, mapped the Huanggangshui Fault offshore segment's geometry and suggested that the Huanggangshui Fault is more likely situated south of Nan'ao Island (Fig. 1), seemingly connecting with the NW-trending Hanjiang Fault on land.

A recent field-based geological mapping study, integrated with shallow reflection seismic data, suggests that NW-trending faults in the Chaoshan Basin near the northwestern extension of the Huanggangshui Fault—including the Rongjiang Fault and the Hanjiang Fault—are active structures. Additionally, a magnitude 6.2 earthquake has been reported to have occurred in 1895 near the Rongjiang Fault (Chen and Huang, 1984). These findings indicate that this region may pose a significant risk of future large earthquakes (Zhang et al., 2003). However, the structural relationship between the Huanggangshui Fault and these NW-trending faults remains poorly understood.

While surface geological surveys and seismicity analyses have provided valuable insights into the geometric characteristics of the seismogenic fault system responsible for past strong earthquakes, they offer limited constraints on the broader tectonic framework governing earthquake generation and occurrence. In particular, the extent and geometry of the NW-trending Huanggangshui Fault on land remain unknown. In this contribution, we construct a three-dimensional upper-crustal shear-wave velocity model using ambient-noise tomography based on a dense seismic node array. This model provides a detailed seismic image with higher resolution on land, enhancing our understanding of the seismogenic structure responsible for strong intraplate earthquakes and offers improved constraints on the onshore geometry of the Huanggangshui Fault compared to Xia et al. (2020).

2. Geological setting and seismicity

2.1. Geological setting

The Shantou region, located in eastern Guangdong Province, South China, lies within the Southeast Coastal Volcanic Rock Belt (Shu, 2012). This area has undergone multiple episodes of intense tectonic and magmatic activities, resulting in extensive fault development and magmatic intrusions (Shu, 2012). The northern Shantou region is primarily underlain by Jurassic sedimentary rocks and Yanshanian granites, while Quaternary sediments are widespread across the coastal plains and river deltas (Fig. 1c). Nan'ao Island, southeast of the Shantou region, is surrounded by seawater and mainly composed of Yanshanian granites (Fig. 1c).

Fault systems comprising multiple NE- and NW-striking faults are well developed in both the coastal and inland areas of the Shantou region, forming a complex intersecting fault network. In the southeastern part of Nan'ao Island, the ENE-striking Littoral Fault intersects with the NW-striking Huanggangshui Fault, forming a junction spatially coincident with the seismogenic zone of the 1918 Nan'ao earthquake (Fig. 1b and c; Xu et al., 2006; Xia et al., 2020). Xu et al. (2006) suggested that the offshore segment of the Huanggangshui Fault is located north of Nan'ao Island based on the isoseismal contour distribution of seismic intensity of the 1918 Nan'ao earthquake. However, Xia et al. (2020), using seismic reflection profiles, mapped the Huanggangshui Fault offshore segment's geometry and found that it is more likely situated south of Nan'ao Island (Fig. 2). Here, we project the Huanggangshui Fault geometry inferred by Xia et al. (2020) onto the topographic map (Fig. 1b and c).

A series of NE-trending faults, including the Chaozhou-Shanwei Fault and the Raoping-Shantou Fault, along with NW-trending faults such as the Rongjiang Fault, the Hanjiang Fault, and the Huangganghe Fault, have developed throughout the Shantou region (Fig. 1b and c; Zhang et al., 2008; Ye et al., 2024). A recent field-based geological mapping study, integrated with shallow reflection seismic data, suggests that these faults are active (Zhang et al., 2018). The NE-trending Chaozhou-Shanwei Fault, located on the northwestern margin of the Shantou Basin, is a major basin-controlling structure and consistently exhibits thrusting behavior, though its dip direction varies across segments (Zhang et al., 2003). The NE-trending Raoping-Shantou Fault, located in the southeastern part of the study area, is mostly concealed beneath Quaternary deposits, with bedrock exposure in the northeastern segment. The fault dips moderately northwest, and surface structural features suggest a compressional shear regime, indicating the fault acts as a thrust fault (Zhang et al., 2008).

The Rongjiang Fault is a major NW-trending structure in the Shantou Basin, mostly concealed beneath Quaternary deposits but influenced by bedrock morphology in its northern segment. Surface geological mapping shows that the fault has experienced both extensional and strike-slip movements (Zhang et al., 2003). Another NW-trending fault (i.e, the Hanjiang Fault), situated along the northeastern margin of the Shantou Basin, exhibits distinct structural characteristics along its length. Its northwestern segment is developed within bedrock, while the southeastern segment remains concealed beneath Quaternary deposits (Zhang et al., 2018). Field measurements indicate a steeply dipping NW-W trending fault plane (20°∠88°), with deformation dominated by extensional brittle faulting, suggesting that the Hanjiang Fault primarily accommodates extensional deformation within the basin (Zhang et al., 2008).

2.2. Seismicity

The Shantou region and the Nan'ao Island near the Littoral Fault have experienced several destructive earthquakes, including two with magnitudes greater than 7.0 in 1600 and 1918, and a magnitude 6.2 earthquake on August 30, 1895 (Chen and Huang, 1984; Xu et al., 2006; Zhang et al., 2008; Sun et al., 2012). The 1918 Nan'ao earthquake, with an estimated focal depth of 15–18 km, was the most devastating seismic event in the region, triggering a tsunami that caused significant casualties and property damage on Nan'ao Island in the Shantou region (Xu et al., 2006; Li et al., 2022). The epicenter of the 1895 *M* 6.2 earthquake approximately located at the southeast of Jieyang County (23°31′N, 116°22′E) (Chen and Huang, 1984). The focal depth of these earthquakes was estimated to be approximately 20 km and these earthquakes caused a large number of house collapses and casualties (Chen and Huang, 1984; Wei et al., 2001).

Over the past 50 years, seismic activity in the Shantou region has remained relatively high, with ten earthquakes of magnitude greater than 4.0 and numerous smaller events clustering near the Littoral Fault

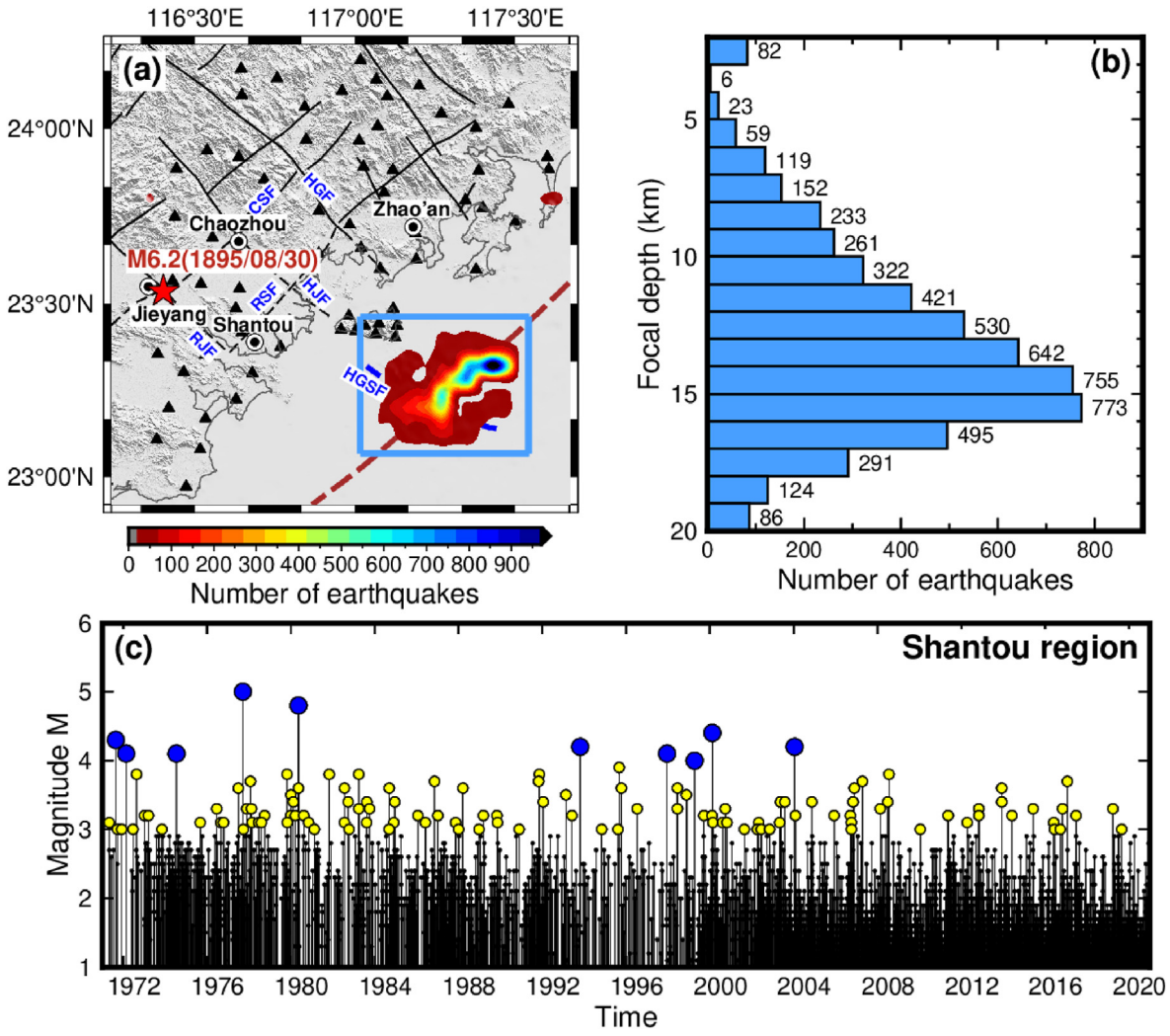

Fig. 2. Seismicity analyses in the Shantou region. (a) Distribution of seismicity density in the study area calculated using a grid size of 0.04° × 0.04°. (b) Histogram of focal depths for earthquakes in the region outlined by the blue rectangle in panel (a). (c) Time series of seismicity from 1971 to 2021 in the Shantou region. The black, yellow, and blue dots indicate the earthquake with magnitudes of $M < 3$, M 3-M 4, and M 4-M 5, respectively.

Zone, predominantly at depths around 15 km (Fig. 2). Zhou et al. (2018) analyzed the *b*-value of the Shantou region using earthquake catalog data from 2008 to 2014, revealing that the *b*-value varies with depth. Notably, in the depth range of 8–15 km, the *b*-value is relatively low (<1.0) (Zhou et al., 2018).

3. Data and methods

3.1. Data

To obtain a three-dimensional upper crustal shear-wave velocity structure in the Shantou region (South China), we deployed a dense seismic array in the study area (indicated by black triangles in Fig. 1b) from December 13, 2023, to January 5, 2024, spanning a total of 21 days (Fig. S1). The array comprised 68 three-component (3C) short-period seismometers, with a corner frequency of 5 s. The average station spacing was approximately 8 km, and the seismometers operated at a sampling rate of 500 Hz.

3.2. Cross-correlation calculation and measurement of surface wave dispersion data

To extract surface waves from recorded ambient noise, we followed the standard seismic data-processing procedure outlined by Bensen et al. (2007) for ambient noise correlation. Initially, we decimated the raw continuous vertical-component ambient noise data from a 500 Hz sampling rate down to 50 Hz for computational efficiency, then divided the data into 2-h segments. Next, we removed the mean and trends, applied a bandpass filter between 0.1 and 10 Hz, and performed time-domain one-bit normalization and spectral whitening on each segment prior to cross-correlation calculation. Cross-correlations were then computed for all station pairs and linearly stacked to obtain the final cross-correlation functions (CCFs) using the SeisNoise.jl program (Clements and Denolle, 2021). This process totally yielded 2 278 CCFs. Fig. 3 shows examples of CCFs for the station-pairs among Station 939 and others at various periods. The apparent velocities of the Rayleigh-wave waveforms range from 2 km/s to 4 km/s at different periods.

Following the stacking of the positive and negative components of the CCFs, we applied the Automatic Frequency-Time Analysis (AFTAN) method (IRIS DMS Product, 2012; Levshin et al., 1972) to extract Rayleigh-wave group and phase velocity dispersion curves. To ensure high-quality dispersion data for subsequent shear-wave velocity inversion, we implemented quality control measures, including a path- cluster analysis (Zhang et al., 2018), and excluded dispersion curves where the station spacing was less than one and a half wavelengths at each period. This criterion helps satisfy the far-field approximation for surface wave propagation (Luo et al., 2015). As a result, we obtained 1497

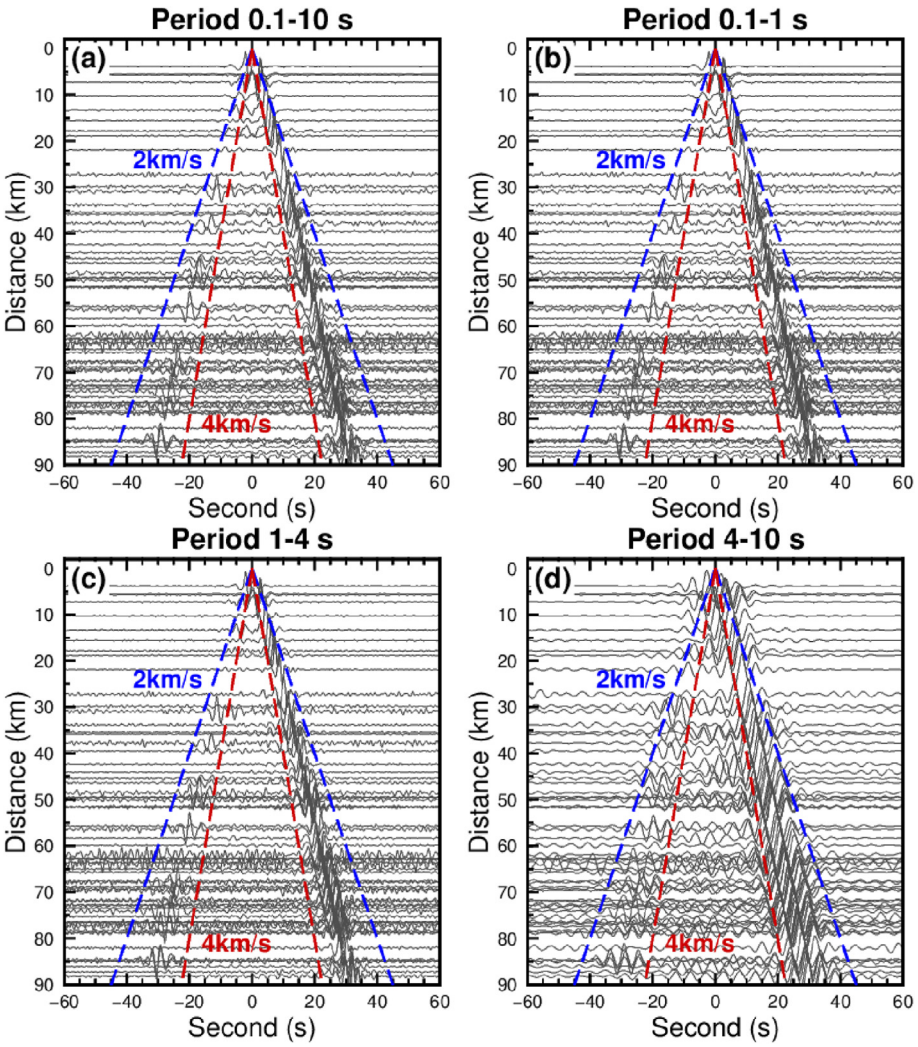

Fig. 3. Example of cross-correlation functions (CCFs) between seismic station 939 and other stations. (a) CCFs filtered at a period band of 0.1–10 s. (b) CCFs filtered at a period band of 0.1–1 s. (c) Same as (b), but for 1–4 s. (d) Same as (b), but for 4–10 s. The red and blue dashed lines represent the apparent velocities of 4 km/s and 2 km/s, respectively.

Rayleigh-wave phase velocity and 1359 group velocity dispersion curves, respectively.

Fig. 4 displays the group- and phase-velocity dispersion measurements along with the number of measurements across different periods. The data reveal an increase in group/phase velocity with period, while the number of dispersion measurements decreases accordingly. Fig. 5 shows ray coverage density maps (with a cell size of 0.04° × 0.04°) for phase and group velocity at 2 s, 4 s, 6 s, and 8 s periods. It's noteworthy that these dispersion measurements are sensitive to shear wave velocity (V_S) down to approximately 15 km depth, as indicated by the sensitivity kernel in Fig. 6.

3.3. Shear-wave velocity inversion

In this study, we applied the Direct Surface Wave Tomography (DSWT) method (Fang et al., 2015) to jointly invert for a 3D V_S model of the study area. A comparison of traditional two-step surface wave tomography and DSWT reveals a strong agreement in the resulting velocity structures (Li et al., 2023). However, this DSWT method incorporates frequency-dependent ray tracing and a wavelet-based sparsity-constrained tomographic inversion, offering the advantage of accounting for the ray path bending effects of surface waves in complex geological structures (Fang et al., 2015).

The residuals between the observed and predicted travel times were determined using an iteratively reweighted least-squares algorithm, as described by Fang et al. (2015):

$$\delta t_i(\omega) = t_i^{\mathrm{obs}}(\omega) - t_i(\omega) = \sum_{k=1}^{K} \nu_{ik} \delta \widehat{S}_k(\omega) \approx -\sum_{k=1}^{K} \nu_{ik} \frac{\delta C_k(\omega)}{C_k^2(\omega)} \tag{1}$$

where $t_i^{obs}(\omega)$ and $t_i(\omega)$ represent the observed and predicted travel times for path i, respectively; $\nu_{ik}(\omega)$ is a bilinear interpolation coefficient for the raypath associated with the ith travel time data; $C_k(\omega)$ and $\delta C_k(\omega)$ are the group/phase velocities and corresponding perturbations of the kth 2D surface grid point, respectively; ω is the angular frequency. In the process of inversion, the group/phase velocity ($C_k(\omega)$) and group-/phase-velocity perturbation ($\delta C_k(\omega)$) at the kth grid point are updated and can be expressed as:

$$\delta C_k(\omega) = \int \left[\left.\frac{\partial C_k(\omega)}{\partial \alpha_k(z)}\right|_{\Theta_k} \delta\alpha_k(z) + \left.\frac{\partial C_k(\omega)}{\partial \beta_k(z)}\right|_{\Theta_k} \delta\beta_k(z) + \left.\frac{\partial C_k(\omega)}{\partial \rho_k(z)}\right|_{\Theta_k} \delta\rho_k(z) \right] dz \tag{2}$$

where $\alpha_k(z)$ $\beta_k(z)$ and $\rho_k(z)$ are the compressional wave speed, shear wave speed, and mass density, respectively. Given that surface waves are

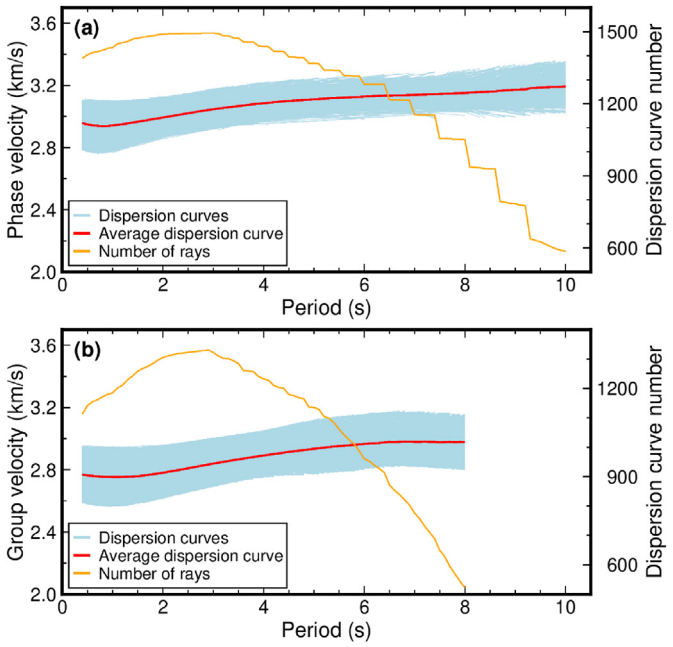

Fig. 4. (a) Phase velocity dispersion curves (light-blue solid lines) extracted from the empirical Green's functions. The red solid line denotes the average phase velocity dispersion curve of all station pairs. The orange solid line marks the number of phase velocity dispersions at each period of 0.4 s–10.0 s. (b) Same as (a), but for group dispersions and the number of group velocity dispersions at each period of 0.4 s–8.0 s.

most sensitive to shear-wave velocity, we can establish a relationship between shear-wave velocity, density, and compressional wave velocity using the empirical relations provided below: V_P (km/s) = 0.9409 + 2.094 V_S – 0.8206 V_S^2 + 0.2683 V_S^3 0.0251 V_S^4 and ρ (g/cm3) = 1.6612 Vp - 0.4721 Vp^2 + 0.0671 Vp^3 - 0.0043 Vp^4 + 0.000106 Vp^5 (Brocher, 2005). Combining Eq. (1) and Eq. (2), we have,

$$\delta t_i(\omega) = \sum_{k=1}^{K}\left(-\frac{\nu_{ik}}{C_k^2(\omega)}\right)\sum_{j=1}^{J}\left[R_\alpha(z_j)\frac{\partial C_k(\omega)}{\partial \alpha_k(z_j)} + R_\rho(z_j)\frac{\partial C_k(\omega)}{\partial \rho_k(z_j)} + \frac{\partial C_k(\omega)}{\partial \beta_k(z_j)}\right]\Bigg|_{\Theta_k}$$
$$\delta\beta_k(z_j) = \sum_{l=1}^{M} G_{il} m_l \tag{3}$$

where θ_k is a 1D reference model. Eq. (3) can be converted into a matrix and the objective function is defined by minimizing the difference between the model prediction times and the observed times:

$$\boldsymbol{\Phi}(\boldsymbol{m}) = \|\boldsymbol{d} - \boldsymbol{G}\boldsymbol{m}\|_2^2 + \lambda\|\boldsymbol{L}\boldsymbol{m}\|_2^2$$

where $\boldsymbol{d}$ is the travel time residual vector for given paths and frequencies, $\boldsymbol{G}$ is the data sensitivity matrix, $\boldsymbol{m}$ is the model parameter vector, $\boldsymbol{L}$ is a model smoothing operator and λ is the weighting parameter balancing data fitting and model regularization (Fang et al., 2015). For more detailed information can refer to Fang et al. (2015).

After many tests with different initial models (Fig. S2), we selected the 1D initial model by linearly interpolating the regional velocity model from Han et al. (2022) at various depths. The model was discretized with a grid spacing of 0.04° in both the longitude and latitude directions (38 × 38 grids) and vertically into layers with a thickness of 0.5 km from the surface to 7 km, and 1 km from 7 km to 20 km depths. Additionally, a damping value of 1.0 was applied to balance velocity perturbations relative to the initial model, and a weight value of 2.0 was selected after a series of tests (Fig. S3).

4. Results

4.1. Checkerboard resolution tests

To assess the resolution and recoverability of the 3D velocity model, we conducted checkerboard resolution tests by introducing alternating positive and negative velocity perturbations of ±10% to the background velocity model. Given the relatively sparse ray path coverage at greater depths, we varied the anomaly sizes with depth, setting them to 16 km ×

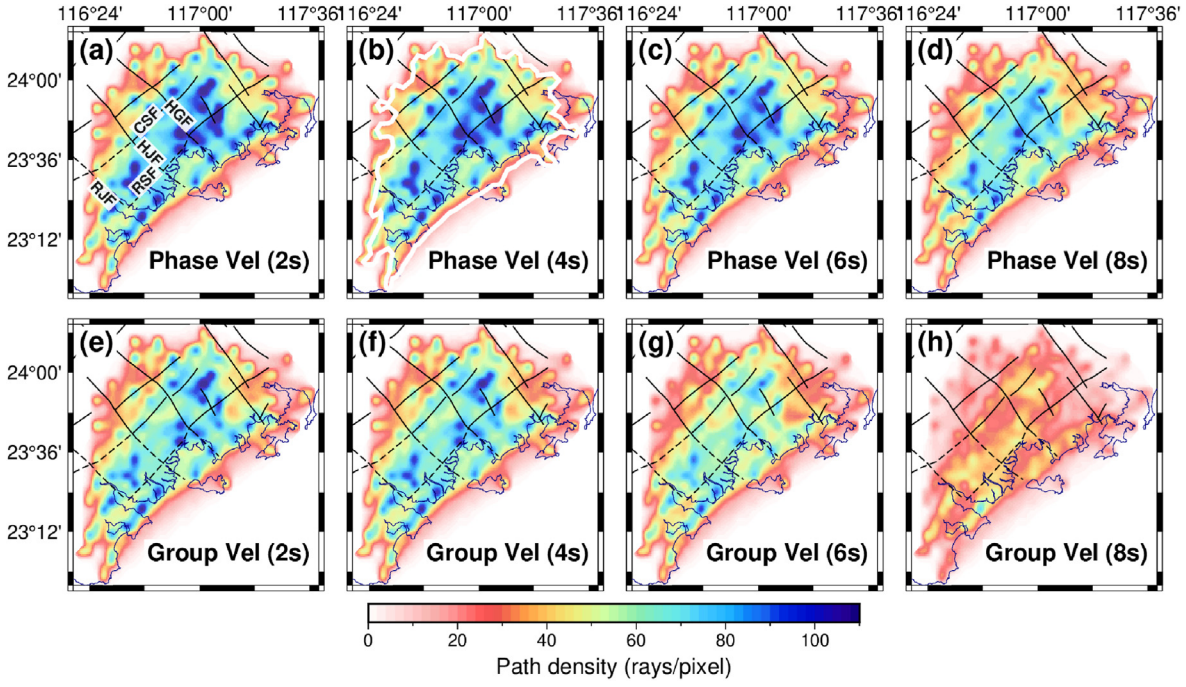

Fig. 5. (a)–(d) Ray coverage density maps for phase velocity at periods of 2 s, 4 s, 6 s and 8 s. The white line in panel (b) denotes the contour line of 30 rays/pixel used for clipping shear-wave velocity maps in Figs. 7–10. The solid black denotes fault lines. The grid size for calculating ray coverage density is 0.04° × 0.04°. (e)–(h) Same as (a)–(d), but for group velocity.

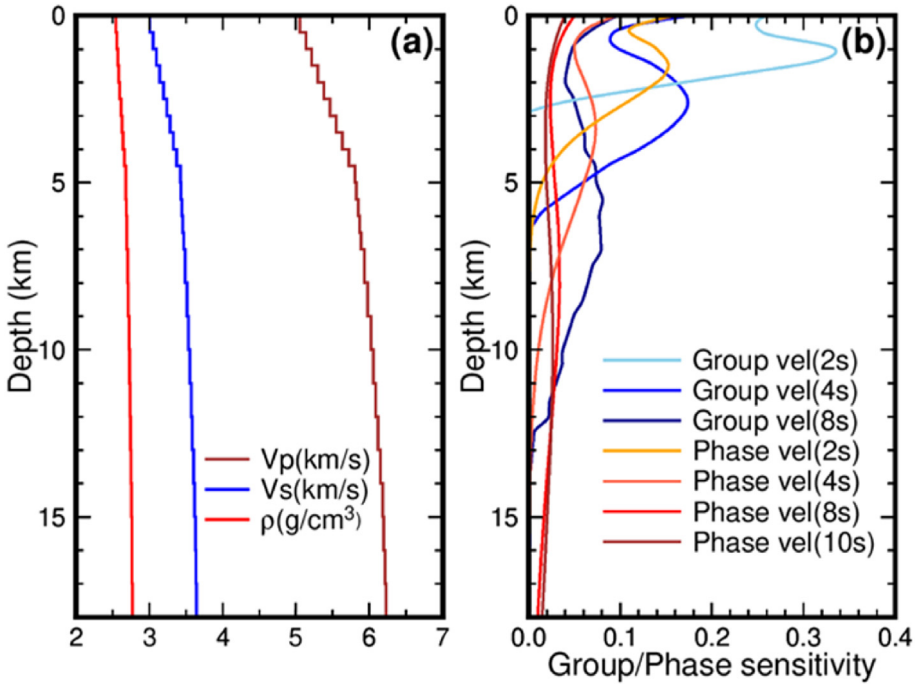

Fig. 6. (a) The initial average compressional-wave velocity model (brown line), shear-wave velocity model (blue line) and density (red line) during shear-wave velocity inversion. The compressional-wave velocity model and density are derived from the shear-wave velocity model using empirical relationships provided by Brocher (2005). (b) The sensitivity kernels of group and phase velocity at different periods to shear-wave velocity. The sensitivity kernels show that the maximum sensitivity depth of phase velocity at both 8 s and 10 s can reach down to 15 km.

16 km and 24 km × 24 km for the depth ranges of 0.5–5 km and 5–15 km, respectively (Fig. 7). We then used Herrmann's (2013) method to calculate synthetic Rayleigh-wave group and phase velocity dispersion curves for the same station pairs as in the observations. To simulate real-world conditions, 2% Gaussian noise was added to the synthetic travel times. Finally, we applied the direct inversion method to retrieve a shear-wave velocity model, which was compared to the input model to evaluate the robustness of the anomalies.

The checkerboard tests (Fig. 7) demonstrate that the input models with varying anomaly sizes at different depths are well recovered, except in the edge areas where reduced ray path density and limited smearing effects diminish resolution. Based on these resolution tests, the following discussion will primarily focus on robust features with sufficient lateral resolution—specifically, 16 km × 16 km from the surface to 5 km depth, and 24 km × 24 km from 5 km to 15 km depth.

4.2. Shear-wave velocity structure

In this study, we have constructed an upper-crustal shear-wave velocity structure in the Shantou region, Guangdong Province (South China), covering the 1895 M 6.2 earthquake. Fig. 8 shows horizontal slices of shear-wave velocity perturbations at depths ranging from 0.5 km to 15 km beneath the Shantou region. The V_S lateral variation from the surface to 1 km depth well aligns with surface lithology (Fig. 8a). The northern area, characterized by Jurassic sedimentary rocks and Yanshanian granite, exhibits relatively high velocities. In contrast, the sediment basin (i.e., the Shantou Basin) in the central and western parts of the study area display relatively low velocities.

The most striking feature in the V_S model is an anomalous low-velocity zone (LVZ) with a size of approximately 20 km × 20 km at depths of 2 to 15 km in the southwestern part of the study area. The V_S perturbations (within this LVZ) reach up to −6% at depths of 2–5 km and −2∼−3% at depths of 5–15 km, in contrast to the relatively high-velocity region in the northern study area. The LVZ disperses along the strike and to the south of the NW-trending Hanjiang Fault, seemingly connecting with the previously identified offshore NW-trending Huanggangshui Fault identified from seismic reflection data (Xia et al., 2020). It is important to note that the perturbation values of −2% to −3% below 5 km depth may be underestimated, as checkerboard tests indicate that the magnitudes of velocity values in our V_S model below 5 km are generally smaller than the actual values due to insufficient ray coverage at longer periods.

To further validate the accuracy and reliability of the low-velocity zone feature identified in our V_S model, we compared the Rayleigh wave phase velocity dispersion curves that traverse both high- and low-shear-wave velocity areas, projecting them onto the velocity perturbation profile at a depth of 4 km. As shown in Fig. 9, the phase velocity dispersion curves passing through the LVZ are consistently lower than those passing through the high-velocity zone. This comparison further confirms the robustness of the LVZ and the high-velocity zone characteristics. Additionally, to assess the potential smearing effect and geometry of the low-velocity zone, we conducted forward modeling tests using different low-velocity zone geometries. We applied a +10% velocity reduction within the low-velocity zones and a −10% increase in the surrounding region, following a procedure similar to the checkerboard tests. The results indicate that while the location of the observed low-velocity zone is well recovered, its shape appears more compact, and its magnitude is reduced in the recovered models (Fig. 10).

5. Discussions

5.1. The causes of the low-velocity zone

We observe an anomalous LVZ approximately at depths ranging from surface to 15 km, covering an area of approximately 20 km × 20 km in the southwestern part of the study area. The velocity variations from the surface to a depth of 2 km align with the lithological variations observed at the surface. Previous geological drilling results indicate that the average thickness of the Quaternary sediments in the study area ranges from 40 to 80 m, with the deepest reaching approximately 160 m (Chen, 1984). Therefore, the LVZ at depths of 2–15 km cannot be explained solely by lithological variations and must involve additional contributing factors.

The subduction of the Paleo-Pacific plate since the Mesozoic and the rifting of the South China Sea during the Cenozoic have profoundly shaped the tectonics of eastern Guangdong. This has resulted in a complex network of intersecting NW-SE and NE-SW trending fault structures (Zhou et al., 2006; Li et al., 2012, 2014, 2019). In the Shantou region, a

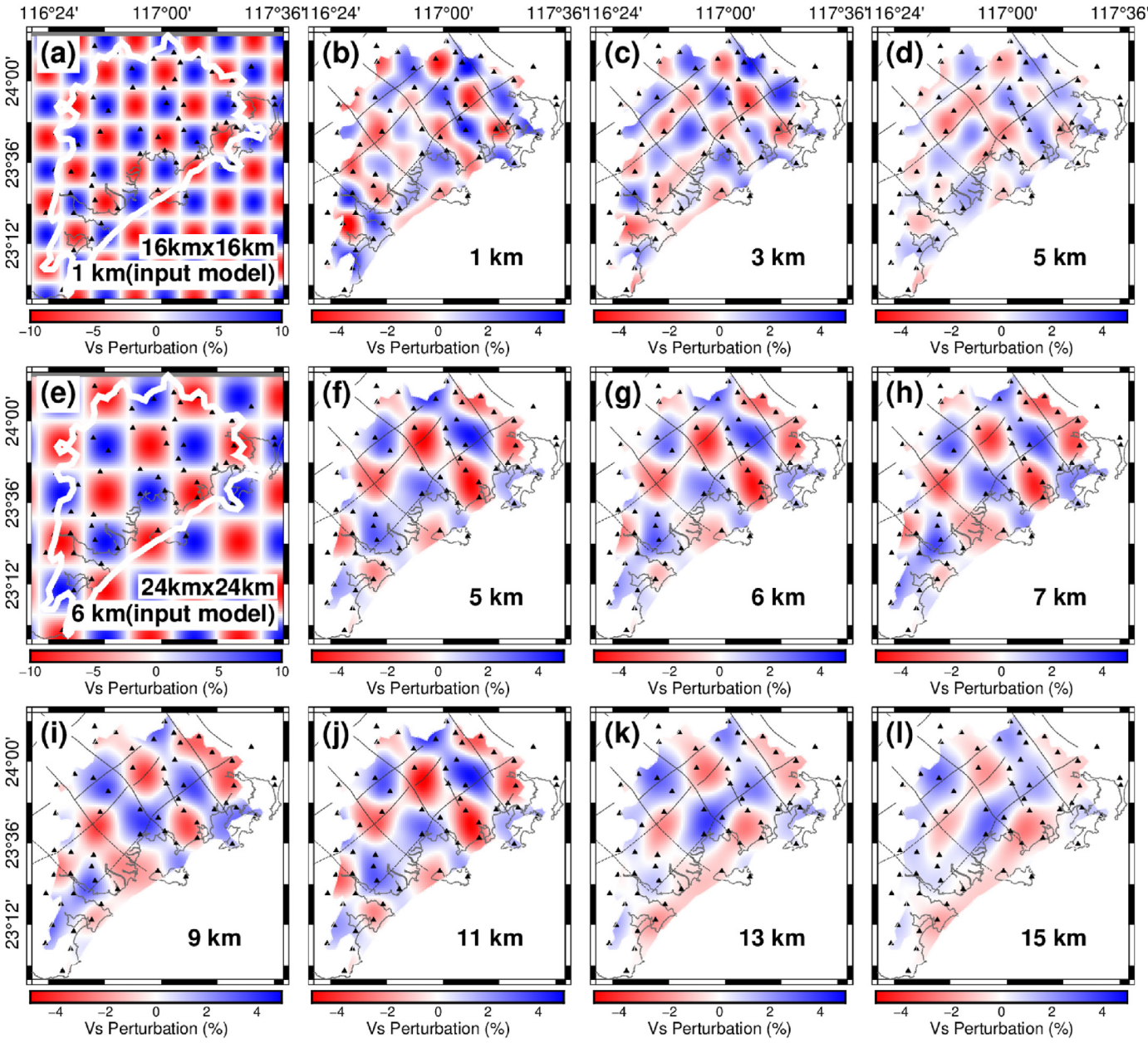

Fig. 7. Lateral checkerboard resolution tests. (a) Input model at a depth of 1 km, with an anomaly size of approximately 16 km. (b)–(d) Recovered models at depths of 1 km, 3 km and 5 km. (e–l) Same as panels (a–d) but for anomaly sizes of approximately 24 km. The ranges of velocity perturbations for both the input and output models are shown, with perturbations of ±10% and ±5% relative to the background velocity, respectively. The value in the lower right corner represents the depth.

series of NE-trending faults (e.g., the Chaozhou-Shanwei Fault and the Raoping-Shantou Fault) intersect NW-trending faults (e.g., the Rongjiang Fault, Hanjiang Fault, and Huangganghe Fault) within the area covered by seismic stations. Recent geological mapping, combined with shallow reflection seismic data, indicates that these faults are active (Zhang et al., 2018). Given this structural complexity, the LVZ may correspond to fault zones within this intersecting fault system.

The LVZ appears to align with the NW-trending Hanjiang Fault, which seemingly connects to the previously identified NW-trending Huanggangshui Fault offshore (Fig. 1), where a similar low-velocity anomaly has been observed (Xia et al., 2020). Previous studies suggest that the Huanggangshui Fault is part of the larger Huanggangshui–Taiwan Narrow Fault system, a 450 km long left-lateral strike-slip fault extending northwest from the Taixi'nan Basin to the southwest of Nan'ao Island (e.g., Xu et al., 2006). Based on this, we interpret the LVZ as representing the fault zone associated with the landward extension of the Huanggangshui Fault's northwestern segment.

The low-velocity zone (LVZ) extends from depths of 2–15 km, with the lowest velocity values observed between 2 km and 5 km (Figs. 11 and 12). This is likely indicative of intense fracturing caused by long-term displacement along the Huanggangshui Fault. Given the station spacing of 8 km, the horizontal resolution of our shear-wave velocity model is approximately 16 km × 16 km. Therefore, the LVZ may consist of multiple fault zones originating from different branches of the Huanggangshui Fault as it separates on land, possibly due to subsurface structural heterogeneity. If this is the case, the NW-trending Hanjiang Fault and Rongjiang Fault, which exhibit dip-slip and strike-slip behaviors at shallow depths, are likely branches of the Huanggangshui Fault that may merge into the LVZ at greater depth. Notably, the seismicity of the Nan'ao offshore region and major earthquakes are not captured in our shear-wave velocity model due to limited ray path coverage resulting from the seismometer distribution. To better constrain fault zones on land,

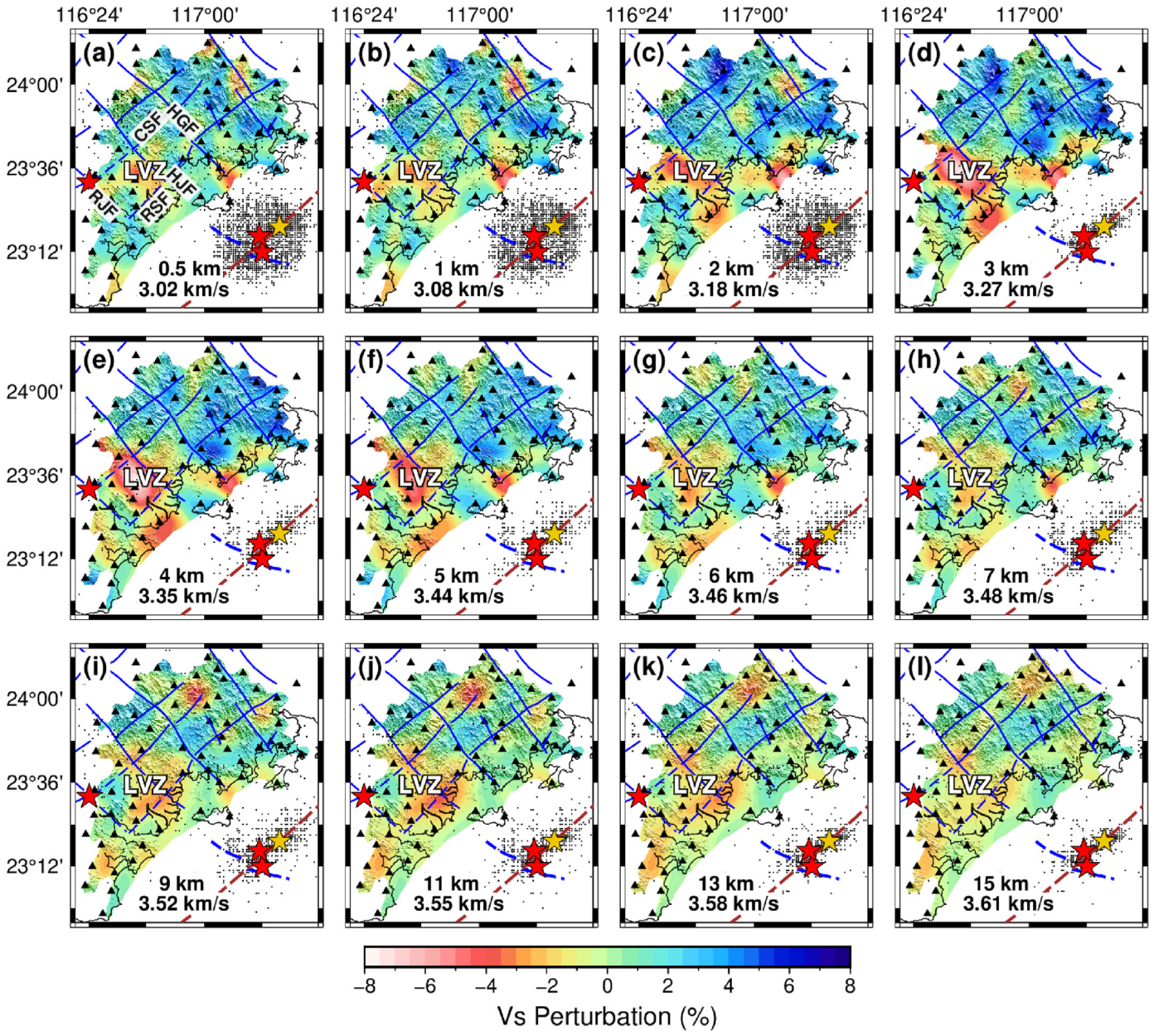

Fig. 8. (a–l) Maps of shear-wave velocity perturbations at depths of 0.5 km, 1 km, 2 km, 3 km, 4 km, 5 km, 6 km, 7 km, 9 km, 11 km, 13 km, and 15 km. Black triangles represent seismic stations. The solid blue lines represent fault lines. The black dots in each panel indicate the locations of earthquakes at corresponding depths within a range of ±2 km. The red star marks the epicenters of strong earthquakes that occurred in the Shantou region, while the gold star denotes a magnitude 5.0 earthquake that occurred on October 23, 2023 in the Shantou region. The brown and blue dashed lines represent the Littoral Fault and the Huanggangshui Fault inferred by Xia et al. (2020), respectively. These maps are clipped at the 30 rays/pixel ray coverage contour for display. In the lower middle part of each figure, the upper value denotes the depth, and the lower value corresponds to the average velocity used for calculating perturbations.

their connections to branches of the Huanggangshui Fault, and their potential roles in generating large earthquakes, high-resolution models incorporating denser nodal arrays across both land and offshore regions are required.

5.2. Implications for the seismogenic structure of strong intraplate earthquakes in the Shantou region, South China

The Shantou region in South China is one of the most seismically active areas in Guangdong Province. Previous studies have reported multiple strong earthquakes with magnitudes exceeding 6.0 in this region (Chen and Huang, 1984; Wei et al., 2001). Investigations of two other seismically active areas in Guangdong Province—the Xinfengjiang Reservoir in Heyuan and the Yangjiang region (Fig. 1a)—suggest that fault intersections and fluid-driven pore pressure increases are key factors contributing to strong earthquakes in the stable South China Block (Li et al., 2024a, 2024b; Dong et al., 2022). Additionally, some studies propose that strong earthquakes in the South China Block are associated with the reactivation of ancient zones of weakness (e.g., Liu, 2001). Understanding the seismogenic structures of these earthquakes is crucial for elucidating their underlying mechanisms.

Previous studies based on the geometry of isoseismal contours (Xu et al., 2006) and seismic imaging (Xia et al., 2020) have demonstrated that a conjugate set of faults controlled the occurrence of the 1918 M 7.3 Nan'ao earthquake: the NE-striking Littoral Fault and the NW-striking Huanggangshui Fault. The Littoral Fault is identified as the dominant seismogenic structure, while the Huanggangshui Fault is considered subdominant. The interaction between the Huanggangshui Fault and the

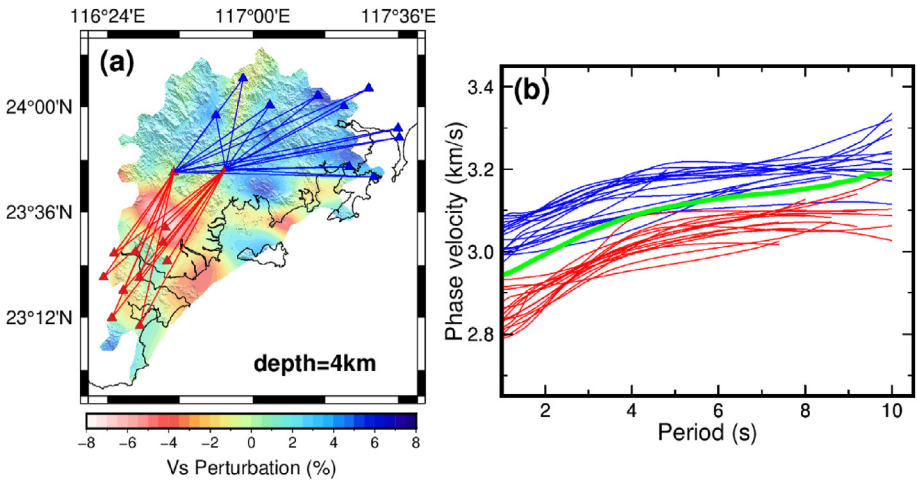

Fig. 9. Validation of the observations of low-velocity zone (LVZ) in the Shantou region using phase velocity dispersions. (a) Selected ray paths of phase velocity dispersion curves that cross the LVZ and high-velocity zones, respectively. The two source stations are located at the center of the Shantou region. Red triangles represent the seismic stations used to extract low phase velocity dispersions, while blue triangles denote stations used for high-velocity phase velocity dispersions. (b) Corresponding phase velocity dispersion curves for low-velocity (red lines) and high-velocity (blue lines) regions. The green line represents the average phase velocity dispersion curve from all station pairs.

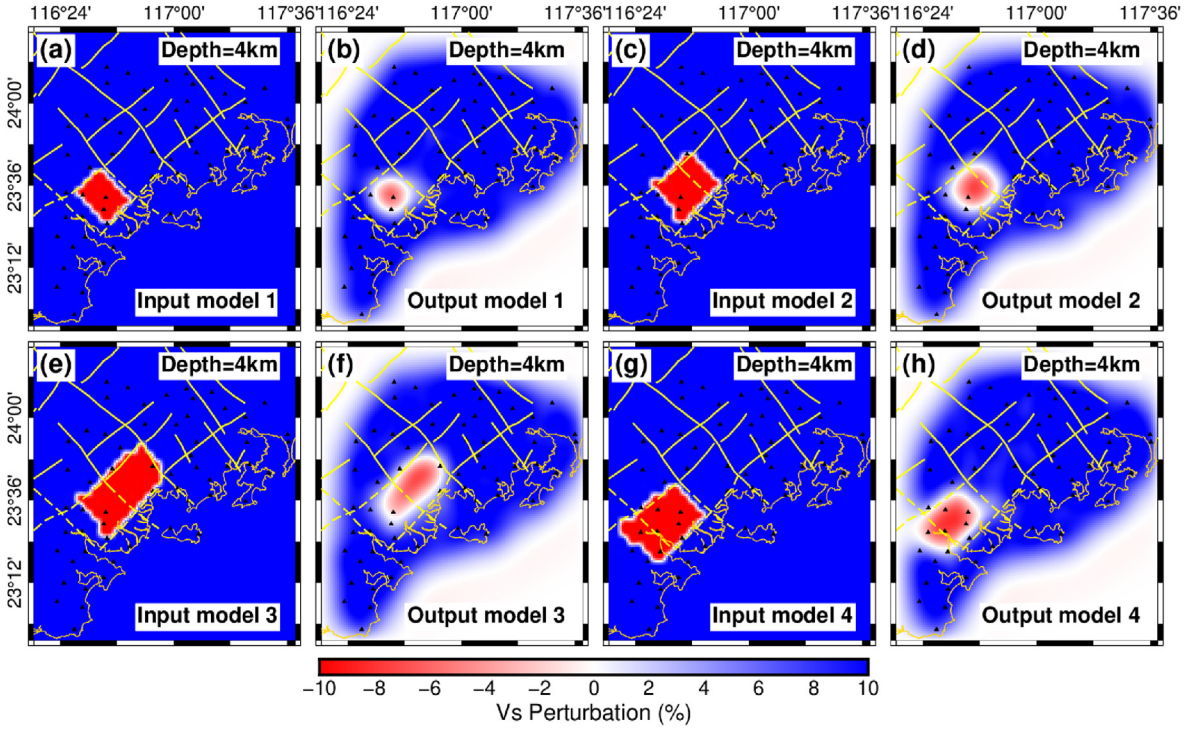

Fig. 10. Forward modeling tests with different geometries for the low-velocity zones. (a) Input model at a depth of 4 km, with an anomaly of −10% velocity perturbation. (b) Recovered model at a depth of 4 km. (c–h) Same as panels (a–b) but with varying geometries for the low-velocity zones. The range of velocity perturbations of the input model and the output model is plotted using ±10% relative to the background velocity. The velocity perturbations for both the input and output models are shown, with a range of ±10% relative to the background velocity.

northern segment of the Taixi'nan Basin Fault has also been implicated in the 1994 *M* 7.3 Taiwan Strait earthquake. Additionally, the 1895 *M* 6.2 earthquake occurred near the low-velocity zone (LVZ) along the inferred land segments of the Huanggangshui Fault. Based on these observations, we propose that the Huanggangshui Fault, which likely comprises the Rongjiang and Hanjiang faults on land, is an active seismogenic fault with significant seismic potential.

Fault intersections appear to be a common tectonic setting for strong earthquakes in Guangdong Province and, more broadly, across South China. The epicenters of the 1969 *M* 6.4 Yangjiang earthquake and the 1962 *M* 6.1 Xinfengjiang Reservoir earthquake were both located at fault zone intersections (e.g., Dong et al., 2022; Li et al., 2024a, 2024b). The 1969 Yangjiang earthquake occurred at the junction of the NW-trending Yangbian fault and the NEE-trending Pingang fault (Wang et al., 2020; Li et al., 2024a), while the 1962 Xinfengjiang Reservoir earthquake was situated at the intersection of a NW-trending hidden fault, the near-NS-trending Shijiao-Xingang-Baitian fault, and the NE-trending Heyuan fault (Ye et al., 2017; Dong et al., 2022). The interaction of the Huanggangshui Fault with other fault systems has created a series of intersection points, where multiple significant earthquakes have occurred. Previous studies demonstrated that fault intersections are often associated with structurally weak zones within the crust, which can facilitate localized stress accumulation, providing a tectonic environment conducive to the generation of strong earthquakes (Xia et al., 2020; Li et al., 2024a, 2024b). Therefore, the LVZ along the Huanggangshui Fault (i.e., the Raojiang Fault and the Hanjiang Fault on land), as well as its

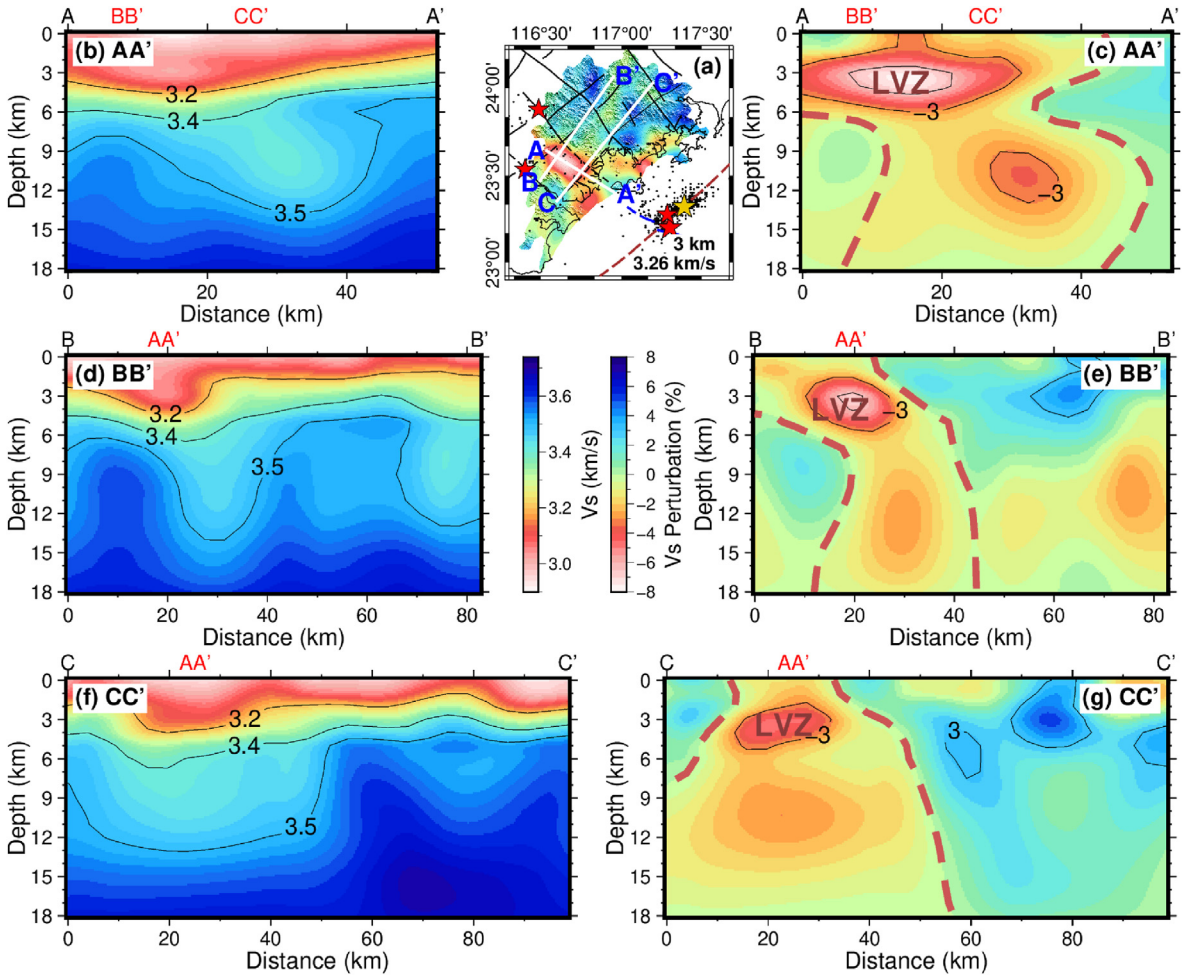

Fig. 11. (a) The shear-wave velocity perturbation maps at 3 km depth, and the locations of cross-sections are shown in panels (b)–(g). The red stars denote the epicenters of strong earthquakes that occurred in the Shantou region. The gold star denotes a magnitude 5.0 earthquake that occurred in the Shantou region on October 23, 2023. (b)–(c) The AA' cross-sections of absolute V_S and V_S anomaly, respectively. The red dashed lines mark the low-velocity zone (LVZ) in the Shantou region. (d)–(e) and (f)–(g) are the same as (b)–(c), but for BB' and CC' cross sections, respectively.

intersections with NE-striking faults (i.e., the Chaozhou-Shanwei Fault and the Raoping-Shantou Fault), may serve as potential sites for future seismic activity and should be given special attention in seismic hazard assessments for the Shantou region.

6. Conclusions

This study employed ambient noise tomography to construct a high-resolution 3D shear-wave velocity (V_S) model for the upper crust in the Shantou region, Guangdong Province (South China). Our model reveals a low-velocity anomaly (LVZ) along the landward segment of the NW-trending Huanggangshui Fault, which, in conjunction with the Littoral Fault, has been linked to the 1918 Nan'ao earthquake. We interpret the LVZ as a fault zone—or possibly multiple fault zones—associated with the Huanggangshui Fault. Given its spatial correlation with several major earthquakes, we suggest that the Huanggangshui Fault, perhaps comprising the Rongjiang Fault and the Hanjiang Fault on land, is an active structure. Its interaction with NE-trending faults (e.g., the Littoral Fault, Chaozhou-Shanwei Fault, and Raoping-Shantou Fault) likely creates a tectonic environment in which stress accumulates at fault intersections, increasing seismic potential. Our findings highlight fault intersections and LVZs as critical areas for seismic hazard assessments, offering valuable insights into intraplate seismic risks in the South China Block and providing a reference for future seismic risk evaluations in the region.

CRediT authorship contribution statement

Lue Yang: Writing – original draft, Data curation, Formal analysis, Investigation, Validation, Visualization. **Lun Li:** Writing – review & editing, Funding acquisition, Conceptualization, Data curation, Formal analysis, Investigation, Project administration, Resources, Supervision, Validation. **Xiuwei Ye:** Writing – review & editing, Investigation. **Jinming Zhang:** Data curation. **Jialong He:** Data curation. **Yuan Gao:** Data curation. **Pengfei Li:** Data curation. **Yu He:** Data curation. **Ziwei Li:** Data curation.

Declaration of competing interest

The authors declare that they have no known competing financial interests or personal relationships that could have appeared to influence the work reported in this paper.

Author agreement and acknowledgment

All authors agree for this publication. The research was funded by the Pearl River Talent Program of Guangdong, China [grant number 2017ZT07Z066], the Innovation Group Project of the South Marine Science and Engineering Guangdong Laboratory (Zhuhai) [grant number 311021003]. Xiuwei Ye acknowledges the support from the Guangdong

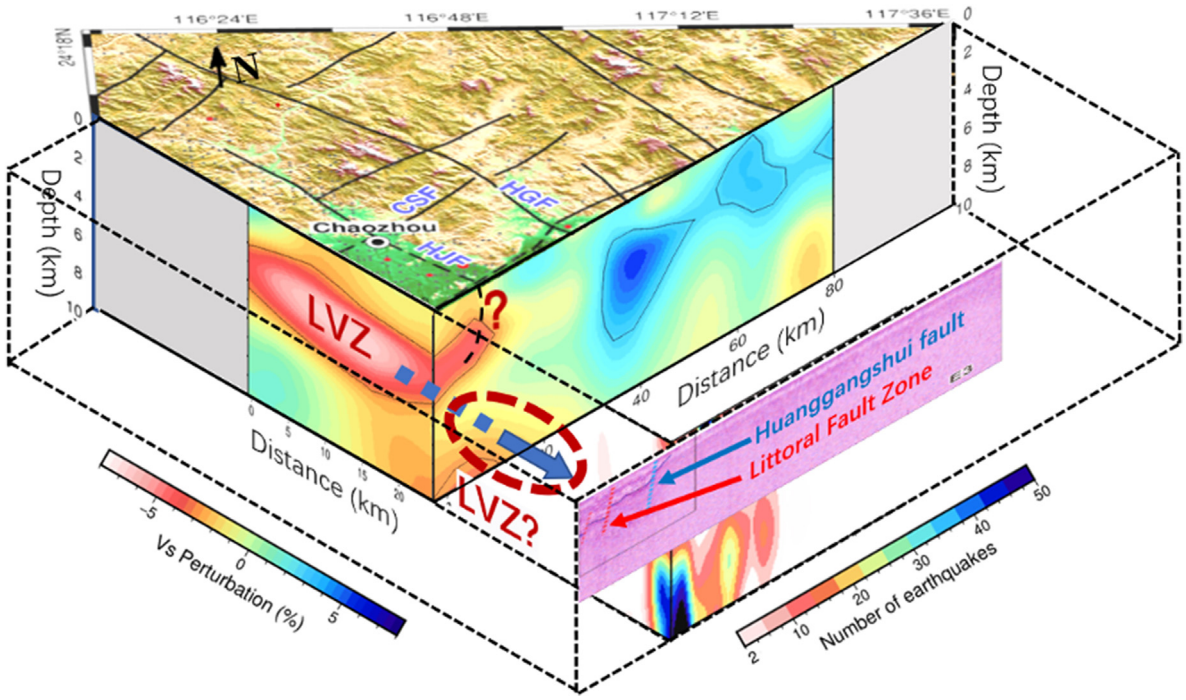

Fig. 12. A 3-D schematic diagram highlighting main seismic observations and interpretation for the cause of intraplate earthquakes in the Shantou region, South China. The two velocity cross sections cross at the low-velocity zone (LVZ) on land. The two seismic density profiles are extended along the velocity profile to the sea and intersect at the intersection of the Huanggangshui fault and the Littoral Fault Zone. The dashed blue arrow and dashed red line indicate a possible low-velocity zone (LVZ) extending from the onshore area to the offshore region. The seismic reflection profile is from Xia et al. (2020), where the red and blue dashed lines represent the inferred Littoral Fault Zone and Huanggangshui fault, respectively. The location of the seismic reflection profile is shown in Fig. 1b, c (E3).

Science and Technology programmer [grant No. 2023A1111120028], the National Key Research and Development Program of China [grant No. 2023YFC3008602].

We thank Editor Prof. Baoshan Wang and two anonymous reviewers for their constructive comments and suggestions. Seismic data processing was conducted using the Seismic Analysis Code (http://ds.iris.edu/ds/nodes/dmc/software/downloads/sac/, last accessed September 2, 2024, Goldstein and Snoke, 2005). The figures were generated with the Generic Mapping Tools (GMT) (https://www.generic-mapping-tools.org/, last accessed September 2, 2024, Wessel et al., 2013). The cross-correlations were calculated with SeisNoise.jl (https://github.com/JuliaSeismo/SeisNoise.jl, last accessed September 2, 2024, Clements and Denolle, 2021). Rayleigh wave phase and group velocity dispersion curves were extracted using the AFTAN program (http://ciei.colorado.edu/Products/, last accessed September 2, 2024, IRIS DMS Product, 2012). The shear-wave velocity model was inverted using the DSurfTomo program (https://github.com/HongjianFang/DSurfTomo, last accessed September 2, 2024, Fang et al., 2015).

Appendix A. Supplementary data

Supplementary data to this article can be found online at https://doi.org/10.1016/j.eqrea.2025.100390.

References

Bensen, G.D., Ritzwoller, M.H., Barmin, M.P., Levshin, A.L., Lin, F., Moschetti, M.P., Shapiro, N.M., Yang, Y., 2007. Processing seismic ambient noise data to obtain reliable broad-band surface wave dispersion measurements. Geophys. J. Int. 169, 1239–1260. https://doi.org/10.1111/j.1365-246X.2007.03374.x.

Brocher, T.M., 2005. Empirical relations between elastic wavespeeds and density in the Earth's crust. Bull. Seismol. Soc. Am. 95, 2081–2092. https://doi.org/10.1785/0120050077.

Chen, W.G., 1984. Characteristics of sedimentary basin development in Chao'Shan area of Guangdong province. South China J. Seismol. 4 (2), 20–30. https://doi.org/10.13512/j.hndz.1984.02.004 (in Chinese).

Chen, E., Huang, Y., 1984. A summary of nineteen strong earthquakes in South China and the continental margin seismic zone in the northern South China Sea. South China J. Seismol. 4 (1), 11–32. https://doi.org/10.13512/j.hndz.1984.01.002.

Clements, T., Denolle, M.A., 2021. SeisNoise. jl: ambient seismic noise cross correlation on the CPU and GPU in Julia. Seismol Res. Lett. 92, 517–527. https://doi.org/10.1785/0220200192.

Deng, Q., 2007. Active Structure Map in China (1:4,000,000). Seismological Press.

Dong, S., Li, L., Zhao, L., Shen, X., Wang, W., Huang, H., Peng, B., Xu, X., Gao, R., 2022. Seismic evidence for fluid-driven pore pressure increase and its links with induced seismicity in the Xinfengjiang reservoir, South China. J. Geophys. Res. Solid Earth 127, e2021JB023548. https://doi.org/10.1029/2021JB023548.

Fang, H., Yao, H., Zhang, H., Huang, Y.-C., Van Der Hilst, R.D., 2015. Direct inversion of surface wave dispersion for three-dimensional shallow crustal structure based on ray tracing: methodology and application. Geophys. J. Int. 201, 1251–1263. https://doi.org/10.1093/gji/ggv080.

Goldstein, P., Snoke, A., 2005. SAC availability for the IRIS community. Incorporated institutions for seismology data management center electronic newsletter [Software]. http://ds.iris.edu/ds/nodes/dmc/software/downloads/sac/.

Han, S., Zhang, H., Xin, H., Shen, W., Yao, H., 2022. USTClitho2.0: updated unified seismic tomography models for continental China lithosphere from joint inversion of body-wave arrival times and surface-wave dispersion data. Seismol Res. Lett. 93, 201–215. https://doi.org/10.1785/0220210122.

Herrmann, R.B., 2013. Computer programs in seismology: an evolving tool for instruction and research. Seismol Res. Lett. 84, 1081–1088. https://doi.org/10.1785/0220110096.

Hui, G., Zhang, P., Li, Z., Wang, W., Hu, L., Li, G., Zhang, Y., Sun, C., Li, S., Liang, H., Li, T., Zheng, J., 2022. Opening of the South China sea marginal basin: insights from the tectonic evolution of the ENE-striking Littoral Fault Zone. Mar. Petrol. Geol. 145, 105854. https://doi.org/10.1016/j.marpetgeo.2022.105854.

IRIS DMS Product, 2012. Western US Ambient Noise Cross-correlations, by Mikhail Barmine and Michael Rtizwoller. published electronically June. incorporated research institutions for seismology [Software]. http://www.iris.edu/dms/products/ancc‐ciei.

Levshin, A.L., Pisarenko, V.F., Pogrebinsky, G.A., 1972. On a frequency-time analysis of oscillations. In: Annales de Geophysique. Centre National de la Recherche Scientifique, pp. 211–218.

Li, S., Santosh, M., Zhao, G., Zhang, G., Jin, C., 2012. Intracontinental deformation in a frontier of super-convergence: a perspective on the tectonic milieu of the South China Block. J. Asian Earth Sci. Oroge. Belts Central Asia: Correla. Connec. 49, 313–329. https://doi.org/10.1016/j.jseaes.2011.07.026.

Li, J., Zhang, Y., Dong, S., Johnston, S.T., 2014. Cretaceous tectonic evolution of South China: a preliminary synthesis. Earth Sci. Rev. 134, 98–136. https://doi.org/10.1016/j.earscirev.2014.03.008.

Li, S., Suo, Y., Li, X., Zhou, J., Santosh, M., Wang, P., Wang, Guangzeng, Guo, L., Yu, S., Lan, H., Dai, L., Zhou, Z., Cao, X., Zhu, J., Liu, B., Jiang, S., Wang, Gang, Zhang, G.,

2019. Mesozoic tectono-magmatic response in the East Asian ocean-continent connection zone to subduction of the Paleo-Pacific Plate. Earth Sci. Rev. 192, 91–137. https://doi.org/10.1016/j.earscirev.2019.03.003.

Li, L., Li, F., Qiu, Q., Li, Z., Zhang, D., Hui, G., 2022. Tsunami simulation of the 1918 Nan'ao earthquake and its implication. Acta Sci. Nat. Univ. Sunyatseni 61, 27–38. https://doi.org/10.13471/j.cnki.acta.snus.2021D043.

Li, L., Cai, C., Fu, Y.Y., Fang, H.J., 2023. Multiple surface wave tomography methods and their applications to the Tibetan Plateau. Rev. Geophys. Plane. Phys. 54 (2), 174–196 (in Chinese).

Li, L., Zhang, J., Shen, X., Wang, X., He, J., Zhao, L., Deng, Z., Gao, R., 2024a. Seismological constraints on the causes of intraplate earthquakes in Yangjiang region, South China. J. Geophys. Res. Solid Earth 129, e2023JB027715. https://doi.org/10.1029/2023JB027715.

Li, L., Shen, X., Dong, S., Liao, J., Zhao, L., 2024b. Crustal seismic velocity structure in the epicenters of strong earthquakes in Guangdong province and their implications for the causes of intraplate earthquakes. Geotect. Metallogenia 48 (3), 420–432. https://doi.org/10.16539/j.ddgzyckx.2024.03.003.

Liu, L., 2001. Stable continental region earthquakes in SouthSouth China. Pure Appl. Geophys. 158, 1583–1611. https://doi.org/10.1007/PL00001235.

Luo, Y., Yang, Y., Xu, Y., Xu, H., Zhao, K., Wang, K., 2015. On the limitations of interstation distances in ambient noise tomography. Geophys. J. Int. 201, 652–661. https://doi.org/10.1093/gji/ggv043.

Ma, J., 1999. Changing viewpoint from fault to block—a discussion about the role of active block in seismicity. Earth Sci. Front. 6 (4), 363–370.

Shu, L., 2012. An analysis of principal features of tectonic evolution in South China Block. Geol. Bull. China 31, 1035–1053. https://doi.org/10.3969/j.issn.1671-2552.2012.07.003.

Sun, J., Xu, H., Zhan, W., Cao, J., 2012. Activity and triggering mechanism of seismic belt along the northern South China Sea continental margin. J. Tropical Oceanograp. 31 (3), 40–47. https://doi.org/10.3969/j.issn.1009-5470.2012.03.006.

Wang, X., Deng, Z., Ye, X., Wang, L., 2020. The study of crustal velocity structure and seismicity in the Yangjiang area of Guangdong province. Seismol. Geol. 42 (5), 1153–1171. https://doi.org/10.3969/j.issn.0253-4967.2020.05.008.

Wei, B., Feng, X., C, D., Huang, R., Wu, S., Ding, X., Hu, J., 2001. Characteristics of Earthquake Activity in the Southeastern Coastal Area. Earthquake Press, Beijing (in Chinese).

Wessel, P., Smith, W.H.F., Scharroo, R., Luis, J., Wobbe, F., 2013. Generic mapping Tools: improved version released (GMT5). EOS Trans. AGU 94 (45), 409–410. https://doi.org/10.1002/2013EO450001 [Software].

Xia, S., Zhou, P., Zhao, D., Cao, J., 2020. Seismogenic structure in the source zone of the 1918 M7.5 Nan'ao earthquake in the northern South China Sea. Phys. Earth Planet. Inter. 302, 106472. https://doi.org/10.1016/j.pepi.2020.106472.

Xie, X., Sun, J., Kang, Y., Xu, H., Xia, S., 2015. Development of offshore ocean bottom seismometer to promote the accuracy of coastal earthquakes relocation——a ML2.8 earthquake in the open sea of nanao. South China J. Seismol. 35 (1), 21–29. https://doi.org/10.13512/j.hndz.2015.01.004.

Xu, H., Qiu, X., Zhao, M., Sun, J., Zhu, J., 2006. Characteristics of the crustal structure and hypocentral tectonics in the epicentral area of Nan'ao earthquake (M7.5), the northeastern South China Sea. Chin. Sci. Bull. 51, 95–106. https://doi.org/10.1007/s11434-006-9095-x.

Xu, H., Ye, C., Qiu, X., Sun, J., Xia, S., 2010. Studies on the Binhai fault zone in the northern South China Sea by the deep geophysical exploration and its seismogenic structure. South China J. Seismol. 30 (S1), 10–18. https://doi.org/10.13512/j.hndz.2010.s1.019.

Ye, X., Deng, Z., Huang, Y., Liu, J., Wang, X., Liu, J., Tan, Z., 2017. The characteristics of 3D P-wave velocity structure of Middle-upper crust and reservoir water infiltration-diffusion in Xinfengjiang Reservoir of Guangdong. Chin. J. Geophys. 60 (9), 3432–3444 (in Chinese).

Ye, X., Lü, Z., Wang, L., Song, J., Duan, Y., Wang, S., Song, X., Zheng, J., Pi, W., 2024. Fine crustal velocity structure revealed by a deep seismic sounding profile of Lianping-Heyuan-Shanwei in the Eastern Guangdong. Chin. J. Geophys. 67 (6), 2304–2321. https://doi.org/10.6038/cjg2022Q0737 (in Chinese).

Zhang, P., Deng, Q., Zhang, G., Ma, J., Gan, W., Min, W., Mao, F., Wang, Q., 2003. Active tectonic blocks and strong earthquakes in the continent of China. Sci. China Earth Sci. 46, 13–24. https://doi.org/10.1360/03dz0002.

Zhang, Z., Pan, H., Wang, J., 2008. Research on historical earthquakes in the eastern Guangdong. Earthq. Res. China 3, 278–287. https://doi.org/10.3969/j.issn.1001-4683.2008.03.010 (in Chinese).

Zhang, Y., Yao, H., Yang, H.-Y., Cai, H.-T., Fang, H., Xu, J., Jin, X., Kuo-Chen, H., Liang, W.-T., Chen, K.-X., 2018. 3-D crustal shear-wave velocity structure of the Taiwan Strait and Fujian, SE China, revealed by ambient noise tomography. J. Geophys. Res. Solid Earth 123 (9), 8016–8031. https://doi.org/10.1029/2018JB015938.

Zhang, Y., Ye, X., Wan, K., Lv, Z., Wen, G., Xu, S., 2024. Fault structure, seismicity, and magmatism of the Littoral Fault zone, northern South China sea: Insights from high-resolution seismic reflection data. Mar. Petrol. Geol. 160, 106605.

Zhao, M., Qiu, X., Ye, C., Xia, K., Huang, C., Xie, J., Wang, P., 2004. Analysis on deep crustal structure along the onshore-offshore seismic profile across the Binhai (Littoral) Fault Zone in northeastern South China Sea. Chin. J. Geophys. 47 (5), 845–852. https://doi.org/10.3321/j.issn:0001-5733.2004.05.016.

Zheng, W.J., Zhang, Z.Q., Hao, M., Chen, J.H., Wang, Q.L., 2022. Physical basis for prediction of continental strong earthquakes: development and prospect of active tectonic block theory. Chin. Sci. Bull. 67 (13), 1352–1361. https://doi.org/10.1360/TB-2021-1025.

Zhou, X., Sun, T., Shen, W., Shu, L., Niu, Y., 2006. Petrogenesis of Mesozoic granitoids and volcanic rocks in South China: a response to tectonic evolution. Episodes J. Intern. Geosci. 29, 26–33. https://doi.org/10.18814/epiiugs/2006/v29i1/004.

Zhou, P., Xia, S., Sun, J., Cao, J., Xu, H., Zhao, F., Chen, C., 2018. Spatial variations of b-values in the coastal area of Guangdong. J. Ocean Univ. China 17, 177–185. https://doi.org/10.1007/s11802-018-3457-2.